An Efficient Spectral-Projection Method for the Navier–Stokes Equations in Cylindrical Geometries

I. Axisymmetric Cases

J. M. Lopez[*,†] and Jie Shen[*]

[*]*Department of Mathematics and* †*Earth System Science Center, Pennsylvania State University,
University Park, Pennsylvania 16802*
E-mail: shen_j@math.psu.edu

An efficient and accurate numerical scheme is presented for the axisymmetric Navier–Stokes equations in primitive variables in a cylinder. The scheme is based on a new spectral-Galerkin approximation for the space variables and a second-order projection scheme for the time variable. The new spectral-projection scheme is implemented to simulate the unsteady incompressible axisymmetric flow with a singular boundary condition which is approximated to within a desired accuracy by using a smooth boundary condition. A sensible comparison is made with a standard second-order (in time and space) finite difference scheme based on a stream function-vorticity formulation and with available experimental data. The numerical results indicate that both schemes produce very reliable results and that despite the singular boundary condition, the spectral-projection scheme is still more accurate (in terms of a fixed number of unknowns) and more efficient (in terms of CPU time required for resolving the flow at a fixed Reynolds number to within a prescribed accuracy) than the finite difference scheme. More importantly, the spectral-projection scheme can be readily extended to three-dimensional nonaxisymmetric cases. © 1998 Academic Press

1. INTRODUCTION

The main purpose of this paper and its sequel is to develop and validate an efficient and accurate numerical scheme for the Navier–Stokes equations (NSE) in cylindrical geometries. We shall restrict ourselves in this paper to the axisymmetric case. The scheme presented here will provide essential ingredients for the three dimensional nonaxisymmetric scheme to be considered in a subsequent study.

The equations governing the flow are the axisymmetric NSE, together with initial and boundary conditions. It is convenient to use a cylindrical coordinate system (r, θ, z). Due to the azimuthal symmetry, the flow depends spatially on only two cylindrical coordinates (r, z). We denote the corresponding velocity and vorticity vectors, in cylindrical coordinates, respectively by

$$\boldsymbol{u} = (u, v, w)^T, \quad \boldsymbol{\omega} = (\xi, \eta, \zeta)^T.$$

For axisymmetric flows, it is usually convenient to introduce a Stokes stream function ψ and to write the Navier–Stokes equations in terms of ψ, η, and $\Gamma = rv$. In this way, the pressure is eliminated via cross-differentiation, and the continuity equation is automatically satisfied. However, such a formulation does not generalize readily to the nonaxisymmetric situation. In order to develop a scheme which can be easily extended to nonaxisymmetric flows, the velocity pressure formulation is adopted. Note, however, that the standard finite difference code that we compare with in Section 4 is in the stream function-vorticity formulation.

The equations governing the axisymmetric flows in the velocity-pressure formulation are

$$u_t + uu_r + wu_z - \frac{1}{r}v^2 = -P_r + \frac{1}{\text{Re}}\left(\tilde{\nabla}^2 u - \frac{1}{r^2}u\right), \tag{1.1}$$

$$v_t + uv_r + wv_z + \frac{1}{r}uv = \frac{1}{\text{Re}}\left(\tilde{\nabla}^2 v - \frac{1}{r^2}v\right), \tag{1.2}$$

$$w_t + uw_r + ww_z = -P_z + \frac{1}{\text{Re}}\tilde{\nabla}^2 w, \tag{1.3}$$

$$\frac{1}{r}(ru)_r + w_z = 0, \tag{1.4}$$

where

$$\tilde{\nabla}^2 = \partial_r^2 + \frac{1}{r}\partial_r + \partial_z^2 \tag{1.5}$$

is the Laplace operator in axisymmetric cylindrical coordinates. The equations (1.1)–(1.4) have been nondimensionalized with the radius of the cylinder R as the length scale and $1/\Omega$ as the time scale, where Ω rad s^{-1} is a characteristic rotation rate of the system. The Reynolds number is $\text{Re} = \Omega R^2/\nu$, where ν is the kinematic viscosity. The flow is governed by another nondimensional parameter, the aspect ratio of the cylinder $\Lambda = H/R$, where H is the height of the cylinder. Therefore, the domain for the space variables (r, z) is the rectangle $(0, 1) \times (0, \Lambda)$. The equations are to be completed with admissible initial and boundary conditions.

Although a finite difference or finite element approximation can be used for the space variables, it appears that a spectral approximation [3, 10] is more appealing in this case because of its ability to resolve thin boundary layers of viscous flows with relatively few collocation points and because of the simplicity of the computational domain. Hence, we shall use a spectral approximation for the space variables.

In order to solve the time dependent problem (1.1)–(1.4) efficiently, it is general practice, especially for spectral approximations, to treat the nonlinear terms explicitly. With this in mind, we still face the difficulty associated with the incompressibility constraint (1.4) which couples the two velocity components u, w and the pressure p. This difficulty can be

overcome by using the so-called influenced matrix method [39]. However, this approach may become prohibitively expensive for long time computations and for three-dimensional simulations. A more efficient way to deal with this coupling is to use a projection (fractional step) method which was originally proposed by Chorin [4] and Temam [37]. In the next section, we will introduce a second-order semi-implicit projection scheme for the axisymmetric NSE. In addition to its remarkable efficiency and accuracy, the scheme has the distinct advantage that it can be easily extended to nonaxisymmetric three-dimensional cases. Note that the apparent coordinate singularity (at $r = 0$) is not of an essential nature and can be handled naturally by using an appropriate variational formulation [30]. In short, we shall develop a spectral-projection scheme which consists of a time discretization by a second-order projection scheme and a space discretization by a spectral-Galerkin method.

We shall use the scheme to simulate the axisymmetric unsteady incompressible flow which is driven by a rotating bottom with constant angular speed. This problem has been extensively studied both numerically (e.g., [2, 5, 16, 18, 20, 21, 24, 26, 34, 38]) and experimentally (e.g., [8, 27, 35, 41]). Problems of this type continue to be of great interest in a wide range of areas, such as the study of wind-forced ocean gyres [12], flow instabilities and the transition to turbulence in rotating systems [11], and the study of boundary layers in rotating systems [14, 17, 19]. Because of its simplicity in formulation and its complexity in dynamics, the present problem is an excellent benchmark problem for axisymmetric flows, just as the driven cavity problem is for two-dimensional flows in Cartesian coordinates. To evaluate the relative merit of our scheme, we shall make a detailed comparison with a standard second-order (in time and space) finite difference scheme (see Appendix A) based on a stream function-vorticity formulation and with available experimental data.

2. A SECOND-ORDER PROJECTION SCHEME FOR TIME DISCRETIZATION

We consider the axisymmetric unsteady incompressible flow which is driven by a rotating bottom with constant angular speed. The boundary conditions for this problem are that the top endwall and the sidewall are stationary, so all components of velocity there are zero, and the bottom endwall is rotating at constant angular speed Ω, so $u = w = 0$ and $v = r$ at $z = 0$. The axis condition is straightforward in the axisymmetric case and is given by $u = v = w_r = 0$ at $r = 0$.

To simplify the presentation, we introduce the notations

$$\tilde{\Delta} = \begin{pmatrix} \tilde{\nabla}^2 - 1/r^2, & 0, & 0 \\ 0, & \tilde{\nabla}^2 - 1/r^2, & 0 \\ 0, & 0, & \tilde{\nabla}^2 \end{pmatrix}, \quad \tilde{\nabla} = \begin{pmatrix} \partial_r \\ 0 \\ \partial_z, \end{pmatrix},$$

$$\mathcal{D} = \{(r, z) : r \in (0, 1) \text{ and } z \in (0, \Lambda)\},$$

$$\Gamma_1 = \{(r, z) : r \in (0, 1) \text{ and } z = 0\}, \quad \Gamma_2 = \{(r, z) : r = 0 \text{ and } z \in (0, \Lambda)\},$$

and rewrite the Eqs. (1.1)–(1.4) in vector form,

$$\boldsymbol{u}_t + N(\boldsymbol{u}) = -\tilde{\nabla}p + \frac{1}{\text{Re}}\tilde{\Delta}\boldsymbol{u},$$

$$\tilde{\nabla} \cdot \boldsymbol{u} := \frac{1}{r}(ru)_r + w_z = 0, \tag{2.1}$$

$$\boldsymbol{u}|_{\partial\mathcal{D}\backslash(\Gamma_1 \cup \Gamma_2)} = \boldsymbol{0}, \quad \boldsymbol{u}|_{\Gamma_1} = (0, r, 0)^T, \quad (u, v, w_r)^T|_{\Gamma_2} = \boldsymbol{0},$$

where $\boldsymbol{u} = (u, v, w)^T$ and $\boldsymbol{N}(\boldsymbol{u})$ is the vector containing the nonlinear terms in (1.1)–(1.3).

To overcome the difficulties associated with the nonlinearity and the coupling of velocity components and the pressure, we propose the following semi-implicit second-order projection scheme for the system of Eqs. (2.1),

$$\frac{1}{2\delta t}(3\tilde{\boldsymbol{u}}^{k+1} - 4\boldsymbol{u}^k + \boldsymbol{u}^{k-1}) - \frac{1}{\text{Re}}\tilde{\Delta}\tilde{\boldsymbol{u}}^{k+1} = -\tilde{\nabla}p^k - (2\boldsymbol{N}(\boldsymbol{u}^k) - \boldsymbol{N}(\boldsymbol{u}^{k-1})),$$

$$\tilde{\boldsymbol{u}}^{k+1}|_{\partial\mathcal{D}\backslash(\Gamma_1\cup\Gamma_2)} = \boldsymbol{0}, \quad \tilde{\boldsymbol{u}}^{k+1}|_{\Gamma_1} = (0, r, 0)^T, \quad (\tilde{u}^{k+1}, \tilde{v}^{k+1}, \tilde{w}_r^{k+1})^T|_{\Gamma_2} = \boldsymbol{0}.$$

(2.2)

$$\frac{1}{2\delta t}(\boldsymbol{u}^{k+1} - \tilde{\boldsymbol{u}}^{k+1}) + \tilde{\nabla}(p^{k+1} - p^k) = \boldsymbol{0},$$

$$\tilde{\nabla} \cdot \boldsymbol{u}^{k+1} = 0,$$

(2.3)

$$(\boldsymbol{u}^{k+1} - \tilde{\boldsymbol{u}}^{k+1}) \cdot \boldsymbol{n}|_{\partial\mathcal{D}} = 0,$$

where δt is the time step, $\boldsymbol{n}$ is the outward normal at the boundary, and $\tilde{\boldsymbol{u}}^{k+1} = (\tilde{u}^{k+1}, \tilde{v}^{k+1}, \tilde{w}^{k+1})^T$ and $\boldsymbol{u}^{k+1} = (u^{k+1}, v^{k+1}, w^{k+1})^T$ are respectively the intermediate and final approximations of $\boldsymbol{u}$ at time $t = k\delta t$.

The scheme is in the same class as the second-order pressure-correction projection scheme of [40] (see also [1]). The linear parabolic operator here is approximated by a second-order backward scheme which appears to be more stable than the Crank–Nicholson scheme, while the nonlinear terms are approximated by a second-order extrapolation to avoid solving a nonlinear system at each time step. It is easy to see that $\tilde{\boldsymbol{u}}^{k+1}$ can be determined from (2.2) by solving three Helmholtz-type equations. Instead of solving for $(\boldsymbol{u}^{k+1}, p^{k+1})$ from the coupled first-order differential equations (2.3), we apply the operator "$\tilde{\nabla}\cdot$" (see the definition in (2.1)) to the first equation in (2.3) to obtain an equivalent system

$$-\tilde{\nabla}^2(p^{k+1} - p^k) = \frac{1}{2\delta t}\tilde{\nabla} \cdot \tilde{\boldsymbol{u}}^{k+1},$$

$$\partial_n(p^{k+1} - p^k)|_{\partial\mathcal{D}} = 0,$$

(2.4)

and

$$\boldsymbol{u}^{k+1} = \tilde{\boldsymbol{u}}^{k+1} - 2\delta t\,\tilde{\nabla}(p^{k+1} - p^k).$$

(2.5)

Thus, $(\boldsymbol{u}^{k+1}, p^{k+1})$ can be obtained by solving an additional Poisson equation (2.4). Note that the equivalence between (2.4)–(2.5) and (2.3) will be no longer valid once the space variables are discretized. However, numerous numerical experiments and the theoretical justification in [33] indicate that this approach does not affect the second-order accuracy in time for the velocity. In the next section, we present an efficient spectral-Galerkin method for solving these equations.

3. SPECTRAL–GALERKIN APPROXIMATIONS FOR AXISYMMETRIC ELLIPTIC EQUATIONS

We first transform the domain $\mathcal{D}$ to the unit square $\mathcal{D}^* = (-1, 1) \times (-1, 1)$ by using the transformations $r = (y + 1)/2$ and $z = \Lambda(x + 1)/2$. Then, at each time step, the systems

(2.2) and (2.4) lead to the following four Helmholtz-type equations:

$$\alpha u - \beta u_{xx} - \frac{1}{y+1}((y+1)u_y)_y + \frac{\gamma}{(y+1)^2}u = f \quad \text{in } \mathcal{D}^*,$$
$$u|_{\partial \mathcal{D}^*} = 0. \tag{3.1}$$

$$\alpha v - \beta v_{xx} - \frac{1}{y+1}((y+1)v_y)_y + \frac{\gamma}{(y+1)^2}v = g \quad \text{in } \mathcal{D}^*,$$
$$v|_{\partial \mathcal{D}^* \setminus \Gamma_1^*} = 0, \quad v|_{\Gamma_1^*} = \frac{1}{2}(y+1). \tag{3.2}$$

$$\alpha w - \beta w_{xx} - \frac{1}{y+1}((y+1)w_y)_y = h \quad \text{in } \mathcal{D}^*,$$
$$w|_{\partial \mathcal{D}^* \setminus \Gamma_2^*} = 0, \quad w_r|_{\Gamma_2^*} = 0. \tag{3.3}$$

$$-\beta p_{xx} - \frac{1}{y+1}((y+1)p_y)_y = q \quad \text{in } \mathcal{D}^*,$$
$$\partial_n p|_{\partial \mathcal{D}^*} = 0. \tag{3.4}$$

In the above, $\Gamma_1^* = \{(x, y) : x = -1 \text{ and } y \in (-1, 1)\}$, $\Gamma_2^* = \{(x, y) : x \in (-1, 1) \text{ and } y = -1\}$, $\alpha = \frac{3}{8}\text{Re}/\delta t$, $\beta = \Lambda^{-2}$, $\gamma = 1$, and f, g, h, q are known functions, depending on the solutions at the two previous time steps.

In [30], an efficient and accurate spectral-Galerkin method was proposed for solving elliptic equations in polar and cylindrical geometries. It was found that the spectral-Galerkin method in [30] is as good, if not more efficient and accurate, as other spectral methods (see, for instance, [7, 23]) which take into account the parity factor (about $r = 0$) satisfied by the solutions. It should also be noted that the clustering of the collocation points near $r = 0$ in this case will not introduce unreasonable time step restrictions as long as the principle linear operator is treated implicitly (cf. [25]).

The spectral-Galerkin method is based on a variational formulation which naturally incorporates the pole conditions and takes care of the coordinate singularity at $r = 0$. For axisymmetric problems, there are no pole conditions but the coordinate singularity at $r = 0$ is still present. The spectral-Galerkin method of [30] can be directly applied to (3.1)–(3.4). We shall discuss the method for solving (3.1) in some detail. The three other equations can be treated similarly.

Let P_K be the space of all polynomials of degree less than or equal to K and $P_{NM} = P_N \times P_M$. We set

$$X_{NM} = \{w \in P_{NM} : w|_{\partial \mathcal{D}^*} = 0\}.$$

Then the spectral-Galerkin method for (3.1) is to find $u_{NM} \in X_{NM}$ such that

$$\alpha((y+1)u_{NM}, v)_{\tilde{\omega}} - \beta\big((y+1)\partial_x^2 u_{NM}, v\big)_{\tilde{\omega}} - \big(((y+1)\partial_y u_{NM})_y, v\big)_{\tilde{\omega}}$$
$$+ \gamma\left(\frac{1}{y+1}u_{NM}, v\right)_{\tilde{\omega}} = ((y+1)f, v)_{\tilde{\omega}} \quad \forall v \in X_{NM}, \tag{3.5}$$

where $(u, v)_{\tilde{\omega}} = \int_{\mathcal{D}^*} uv\omega(x)\omega(y)\,dx\,dy$ with $\omega(s)$ to be respectively 1 or $(1 - s^2)^{-1/2}$, depending on whether Legendre or Chebyshev polynomials are used. The Eq. (3.5) is derived by first multiplying (3.1) by $(y + 1)\omega(x)\omega(y)$ and then integrating over $\mathcal{D}^*$. The

multiplication by $(y + 1)$ is natural since the Jacobian of the transformation from the Cartesian coordinates to cylindrical coordinates is $r = ((y + 1)/2)$ in the axisymmetric case. Since $u_{NM} = 0$ at $y = -1$, we see that all terms in (3.5) are well defined and that no singularity is present.

The efficiency of the method depends on the choice of basis function for X_{NM}. The general strategy for choosing basis functions was discussed in [30, 32]. For this problem, it is easy to verify that

$$X_{NM} = \text{span}\{\phi_i(x)\rho_j(y) : i = 0, 1, \ldots, N - 2; \ j = 0, 1, \ldots, M - 2\},$$

with $\phi_l(s) = \rho_l(s) = p_l(s) - p_{l+2}(s)$, where $p_l(s)$ is either the lth degree Legendre or Chebyshev polynomial. Setting

$$u_{NM} = \sum_{i=0}^{N-2} \sum_{j=0}^{M-2} u_{ij}\phi_i(x)\rho_j(y),$$

and

$$
\begin{aligned}
a_{ij} &= \int_{-1}^{1} \phi_j(x)\phi_i(x)\omega(x)\,dx, \\
b_{ij} &= -\int_{-1}^{1} \phi_j''(x)\phi_i(x)\omega(x)\,dx, \\
c_{ij} &= \int_{-1}^{1} (y + 1)\rho_j(y)\rho_i(y)\omega(y)\,dy, \\
d_{ij} &= -\int_{-1}^{1} \left((y + 1)\rho_j'(y)\right)'\rho_i(y)\omega(y)\,dy, \\
e_{ij} &= \int_{-1}^{1} \frac{1}{y + 1}\rho_j(y)\rho_i(y)\omega(y)\,dy, \\
f_{ij} &= \int_{\mathcal{D}} (y + 1)f\,\rho_j(y)\phi_i(x)\omega(x)\omega(y)\,dx\,dy,
\end{aligned}
\tag{3.6}
$$

and letting A, B, C, D, E, F, and U be the corresponding matrices with entries given above. Then, (3.5) is equivalent to the following matrix system:

$$\alpha AUC + \beta BUC + AUD + \gamma AUE = F. \tag{3.7}$$

Note that e_{ij} is well defined despite the term $1/(y + 1)$ since $\rho_i(-1) = 0$. In the Legendre case, the matrices A, B, C, D, and E are all symmetric and sparsely banded, while in the Chebyshev case, only A, C, and E are symmetric and sparsely banded, but B and D are respectively full triangular and Hessenburg matrices with special structures (see [30] for more details). Hence, (3.7) can be efficiently solved by using the matrix diagonalization method [22, 30] at a cost of $4NM \min(N, M) + O(NM)$ operations. Note, however, that in the Legendre case this operation count can be reduced to $O(NM \log(N + M))$ (see [32] for further details).

4. NUMERICAL RESULTS AND COMPARISON WITH A STANDARD
FINITE DIFFERENCE METHOD

4.1. *Treatment of the Singular Boundary Condition*

The boundary condition for v is discontinuous at the lower right corner ($r = 1, z = 0$). This is a physical singularity and it represents the fact that in this enclosed system, all the vortex lines emanate from the rotating endwall, and, since they cannot terminate on the stationary walls nor in the interior of the fluid, they all terminate at the corner singularity. The form of this singularity is kinematic, it does not change with Re.

We should emphasize that this singular boundary condition is a mathematical idealization of the physical situation, where there is a thin gap (usually on the order of $0.02R$, as in [35]) over which v adjusts from 1.0 on the edge of the rotating endwall to 0.0 on the sidewall. Therefore, it is appropriate to use a regularized boundary condition (so that v is continuous) which is representative of the actual gap between the rotating endwall and the stationary sidewall in experiments.

In finite difference or finite element schemes, the singularity is usually regularized over a few grid spacings in the neighborhood of the corner. However, this simple treatment leads to a mesh-dependent boundary condition which in turn results in mesh-dependent solutions which prevents a sensible comparison between solutions with different meshes. Essentially, the grid spacing represents the physical gap size. Alternative schemes have successfully treated singularities by, for example, using crack tip singular finite elements in the neighborhood of the singularity (see, for example, [9]), or by adding a Navier slip coefficient (see, for example, [28]).

The singular boundary condition at $r = 1$ is

$$v(z) = 1 \quad \text{at } z = 0, \quad v(z) = 0 \quad \text{for } 0 < z \le \Lambda,$$

which is similar to that of the driven cavity problem. Unless this singularity is treated appropriately, spectral methods may have severe difficulty dealing with it. In the past, most computations with spectral methods avoided this difficulty by using regularized boundary conditions which, unfortunately, do not approximate the physical boundary condition (e.g., [6, 31]). The authors of [15], used an *ad hoc* procedure which corresponds to approximating v by a polynomial v_M (of degree M) such that $v_M(z_0) = 1$, $v_M(z_1) = 0.3$, and $v_M(z_i) = 0$ for $i = 2, \dots, M$, where $\{z_i\}$ are the Gauss–Lobatto collocation points in $[0, \Lambda]$. Although reasonably accurate results were obtained by using this procedure, it will produce mesh-dependent solutions and, furthermore, it introduces nonsmoothness into the computed solutions (see Fig. 4.2). Note that alternatively it is also possible to treat the singularity by subtracting the leading singular part as in [29].

We propose using the boundary layer function,

$$v_\varepsilon(z) = \exp\left(-\frac{2z}{\Lambda \varepsilon}\right),$$

which has the ability to approximate the singular boundary condition to within any prescribed accuracy. Outside a boundary layer of width $O(\varepsilon)$, $v_\varepsilon(z)$, converges to $v(z)$ exponentially as $\varepsilon \to 0$. However, for a given ε, approximately $\varepsilon^{-1/2}$ collocation points are needed to represent the boundary layer function v_ε. In other words, for a fixed number of modes M,
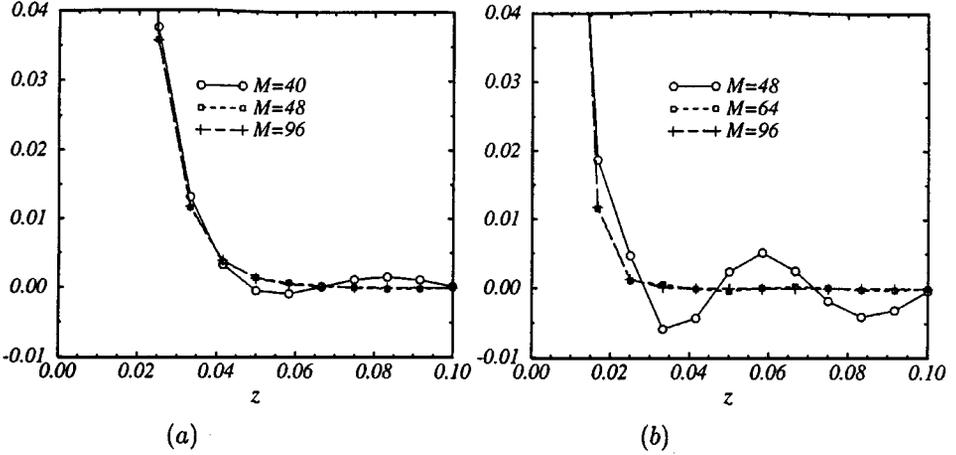
FIG. 1. Variation of $I_M v_\varepsilon$ (with $\Lambda = 2.5$) in the vicinity of the singularity at $z = 0$ for (a) $\varepsilon = 0.006$ and (b) $\varepsilon = 0.003$, and various M as indicated.

we can only use $\varepsilon \geq \varepsilon(M)$, where $\varepsilon(M)$ can be approximately determined by comparing $I_M v_\varepsilon$ and v_ε, where $I_M v_\varepsilon$ is the polynomial interpolation of v_ε at the Gauss–Lobatto points.

Although it is virtually impossible to match the exact physical condition in the experimental gap region, the function v_ε with $\varepsilon = 0.006$ does provide a reasonable representation of the experimental gap. The function v_ε can be resolved spectrally with $M \geq M_\varepsilon$ modes, where M_ε is such that $I_M v_\varepsilon$ for a given ε is nonoscillatory. Due to the nonlinear term v^2/r in (1.1), we also require that $I_M v_{\varepsilon/2}$ be nonoscillatory (since $(v_\varepsilon)^2 = v_{\varepsilon/2}$). Figure 1a shows $I_M v_{0.006}$ for various M. It is clear that $I_{48} v_{0.006}$ is nonoscillatory. However, from Fig. 1b we see that $I_{48} v_{0.003}$ is oscillatory near $z = 0$, while $I_{64} v_{0.003}$ is not. Thus, $M \approx 64$ is required for $\varepsilon = 0.006$.

Figure 2 shows plots of the solution for Stokes flow (Re $= 0$) for this problem. The governing equations (1.1)–(1.4) in the case Re $= 0$ reduce to

$$\tilde{\nabla}^2 v - (1/r^2)v = \tilde{\nabla}^2 \Gamma = 0,$$

with $\Gamma = 0$ on the axis, top endwall, and sidewall, and $\Gamma = r^2$ on the rotating bottom endwall. The singular boundary condition on the sidewall has been regularized in Fig. 2a with $v_{0.006}$ and in Fig. 2b with the *ad hoc* method. For the solution of the Stokes problem with $\varepsilon = 0.006$, we judge that the error is acceptably small at $M = 64$ and is very small at $M = 80$. The measure of error used here is the largest value of negative Γ of the computed solution at the grid points of a uniform 201×501 mesh; the true solution has $\Gamma \geq 0$. These values are listed in Table 1. In contrast, with the *ad hoc* method the error does not decrease as M increases and the computed solutions exhibit large errors for all values of M considered.

4.2. Numerical Results and Discussion

In order to make sensible comparisons between the spectral code and the finite difference code (see Appendix A) and between cases with different finite difference grids, $v_\varepsilon(z)$ is
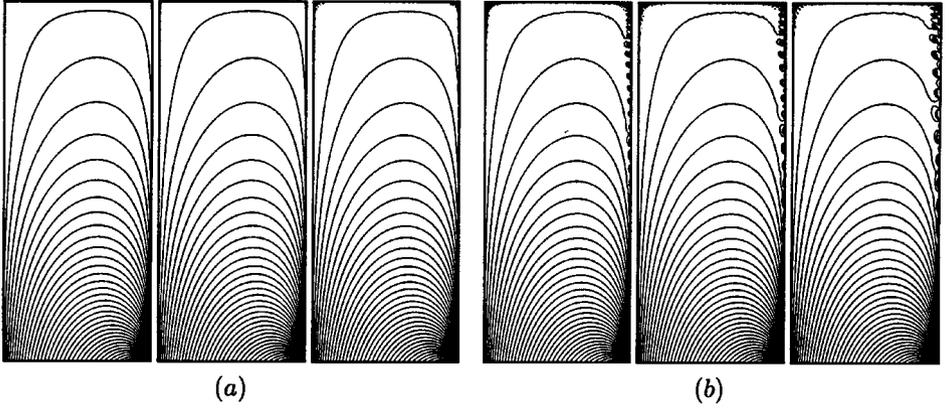
FIG. 2. Contours of Γ for Stokes flow (Re $= 0$), using (a) $v_{0.006}$ and (b) the *ad hoc* regularization of the corner singularity. The leftmost plot in each set has $N = 56$, $M = 80$, the middle plots have $N = 48$, $M = 64$, and the right plots have $N = 40$, $M = 48$. All have been projected on to 201 uniform radial locations and 501 uniform axial locations.

used here as the boundary condition on v at $r = 1$ in both codes, and the single value of $\varepsilon = 0.006$ is used throughout. Note that ε can be regarded as another dynamic parameter representative of the physical gap at the corner.

We use the spectral-projection scheme and the finite difference code to solve our problem at two different Reynolds numbers with $\Lambda = 2.5$. The first corresponds to a steady solution at Re $= 2494$. This Re is large enough that boundary layers are thin (thickness $O(\text{Re}^{-1/2})$), but small enough that the flow becomes steady. The primary interest here is to determine the level of spatial resolution required for an asymptotically grid/mode independent solution for each scheme. We shall, however, also consider the transients during the evolution to the steady state, as the time-accuracy of the schemes is also of interest. The second test case is the periodic flow at Re $= 2765$. We compare both the transients and the limit cycle solutions from the two schemes. Both test cases are well documented, both experimentally [8] and numerically [16, 18]. Recent experiments [35] indicate that the flow is unstable to nonaxisymmetric perturbations for Re ≥ 3500, so we leave the consideration of higher Reynolds number cases to the subsequent paper dealing with nonaxisymmetric three-dimensional flows.

For all cases, we use rest as the initial condition and impulsively start the bottom endwall rotating at $t = 0$. Although the temporal singularity at $t = 0$ does affect the initial transients, Heywood and Rannacher [13] have proven that it has no effect on the characteristics of the final asymptotic solutions.

TABLE 1

Largest Negative Values of Γ on the Grid Points of a 201 $\times$ 501 Uniform Mesh, Corresponding to the Solutions for Stokes Flow Shown in Fig. 2

N, M	min(Γ) with $\varepsilon = 0.006$	min(Γ) with *ad hoc* b.c.
56, 80	-2.472×10^{-6}	-4.786×10^{-3}
48, 64	-9.002×10^{-6}	-6.510×10^{-3}
40, 48	-1.633×10^{-4}	-6.444×10^{-3}
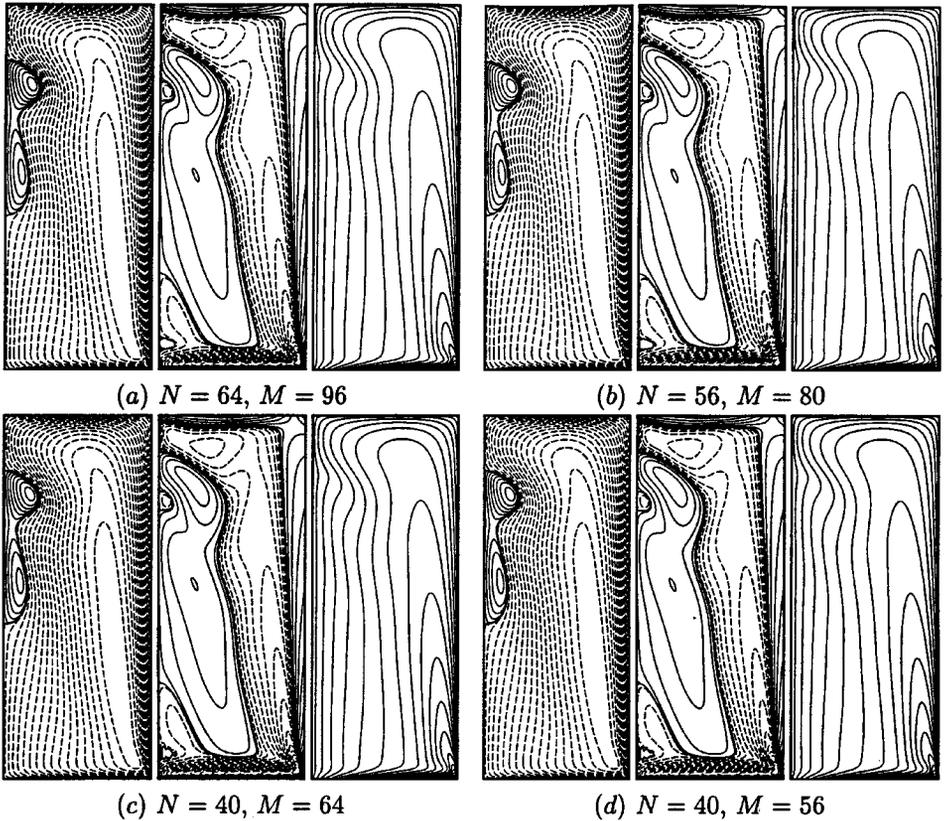
FIG. 3. Contours of ψ, η, and Γ for Re $= 2494$ and $\Lambda = 2.5$ at $t = 3000$. Solutions are from spectral computations with $\delta t = 0.04$ and $\varepsilon = 0.006$ and N and M as indicated. All have been projected on to 201 uniform radial locations and 501 uniform axial locations.

We begin by determining the level of resolution needed for a spectral computation of the case with Re $= 2494$, $\Lambda = 2.5$, and $\varepsilon = 0.006$. From the Stokes flow problem, we have seen that for $\varepsilon = 0.006$, the proper treatment of the singularity at the corner requires $M \approx 64$. Figure 3 shows the solutions at $t = 3000$, which are essentially at steady state (i.e., changes in any quantity being less than 1 part in 10^5 between successive time steps), from spectral computations using a variety of resolutions. The plots are produced by projecting the spectral solutions onto 201 radial and 501 axial uniformly distributed physical locations (both ψ and η are determined spectrally from $\boldsymbol{u}$). A comparison of these contours shows very little difference, except for some oscillations in η, the azimuthal component of the vorticity, near the axis where $\eta \approx 0$. These oscillations are considerably reduced with an increase in the number of spectral modes used. Figure 4a is a detail of the time history of the azimuthal velocity at $r = 1/2$, $z = \Lambda/2$, a point which is not particularly sensitive. It illustrates the convergence of the solutions as N and M are increased. It also demonstrates that the temporal characteristics of the flow transients are not sensitive to the level of spatial resolution.

We have also computed cases with the same spatial resolution, but with two different temporal resolutions. Computations with $\delta t = 0.04$ and $\delta t = 0.01$ agree to four or five
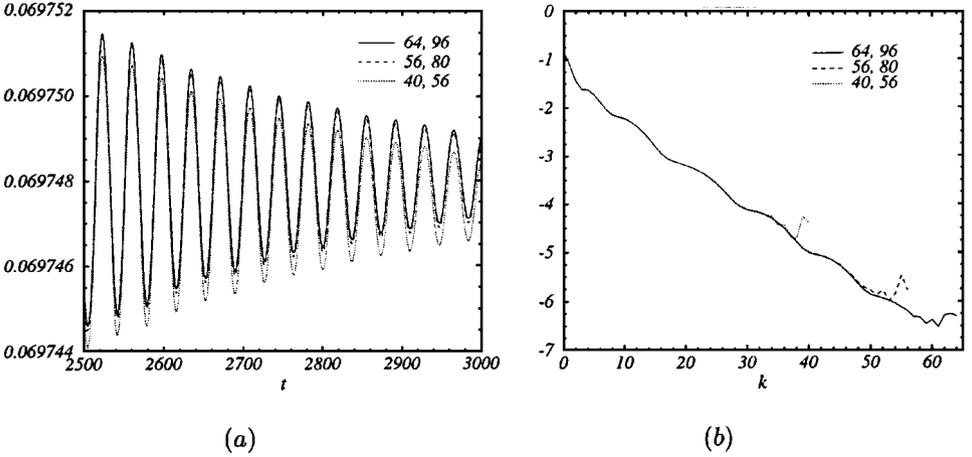
FIG. 4. (a) Detail of the time history of $v(r = 1/2, z = \Lambda/2)$ for Re $= 2494$, $\Lambda = 2.5$, from spectral computations with $\varepsilon = 0.006$, and N and M as indicated. (b) $\log(E_k)$ versus k, where E_k is the energy contribution, from v, from different levels of modes ($k = 0, \ldots, M$), corresponding to the solutions in (a).

digits, which is of the same order as the time discretization error, and corresponding plots of the form shown in Fig. 4a are indistinguishable for these cases.

In Fig. 4b, we show how the energy contribution E_k, from different levels of modes ($k = 0, \ldots, N$) decreases as k increases. E_k is defined as the sum of the energy contribution from the modes v_{ik} for $i = 0, \ldots, M-N+k$ and $v_{k,j}$ for $j = 0, \ldots, k$ (v_{ij} are the coefficients of the Legendre expansion of v). The exponential decrease of E_k exhibited in Fig. 4b is a good indication that the solutions are well resolved. Note also that except for a few of the highest modes, the energy distributions of differently resolved solutions overlap each other, providing another indication of their convergence.

From these convergence tests, we conclude that for $N = 40$, $M = 56$, $\delta t = 0.04$, we already have very good results for the primitive variables (u, v, w) but the approximation for the azimuthal vorticity η at this resolution is not acceptable. We recall that η is computed by taking derivatives of u and w, so it is not unexpected that η requires more resolution than the velocity. At $N = 56$, $M = 80$, $\delta t = 0.04$, the η contours are very smooth and this solution can be taken as being independent of discretization. We use this solution to compare with the finite difference solutions.

The finite difference code has been used with both uniform and stretched grids. Solutions on stretched grids with $N = 60$, $M = 150$, $\delta t = 0.02$ and $N = 120$, $M = 300$, $\delta t = 0.005$ are shown in Fig. 5. Comparing the two solutions visually, there are only very minor differences detected, and a visual comparison with the spectral solutions in Fig. 3 also shows very small differences. The overall structure of the solutions, the shape of the recirculation zone, and the vorticity distributions all agree. The finite difference solutions, even on the coarser $N = 60$, $M = 150$ uniform grid (not shown), are all very smooth; however, a detailed comparison shows that the smoothness of a solution is not a sufficient indicator of convergence to a grid independent solution. In Fig. 6, we show the time histories of $v(r = 1/2, z = \Lambda/2)$ of several computed solutions. We observe that the transients following the impulsive start from rest agree well at the beginning. The difference between solutions shows up at later times, as illustrated in Fig. 6b. As the
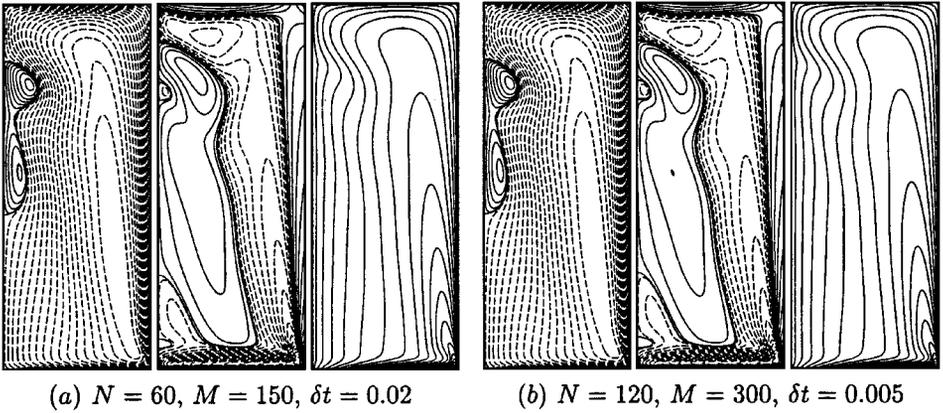
(a) $N = 60$, $M = 150$, $\delta t = 0.02$ (b) $N = 120$, $M = 300$, $\delta t = 0.005$

FIG. 5. Contours of ψ, η, and Γ for Re $= 2494$ and $\Lambda = 2.5$ at $t = 3000$. Solutions are from finite difference computations with $\varepsilon = 0.006$ on the stretched grid and N, M, and δt as indicated.

spatial resolution of the finite difference solutions increases, they converge to the spectral solution.

As a further illustration of the convergence of the solutions, we list in Tables 2 and 3 the values and locations (on a 201×501 uniform physical grid for the spectral solutions, and on their own grids for the finite difference solutions) of three local maxima and minima of ψ and η. It can be concluded that the spectral-projection scheme with 57×81 modes provides significantly more accurate results than the (stretched) finite difference scheme with 121×301 grid points.

We now turn to the unsteady case with Re $= 2765$. The structure and dynamics of this case have been discussed in detail in [8, 18]. Here, we compare the results of computations
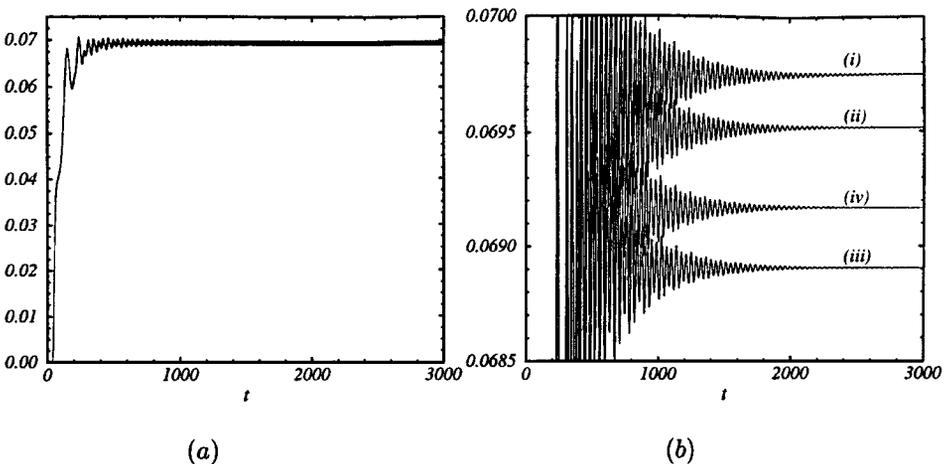

(a)   (b)

FIG. 6. Time histories of $v(r = 1/2, z = \Lambda/2)$ for Re $= 2494$ from computations with (i) the spectral code using $N = 56$, $M = 80$, and $\delta t = 0.04$, and the finite difference code using the stretched grids with (ii) $N = 120$, $M = 300$, $\delta t = 0.005$, (iii) $N = 60$, $M = 150$, $\delta t = 0.02$, and (iv) using a uniform grid with $N = 120$, $M = 300$, $\delta t = 0.01$; all computations had $\varepsilon = 0.006$. (b) is a close-up view of (a).

TABLE 2
Local Maxima and Minima of ψ and Their Locations for Re = 2494, Λ = 2.5, and ε = 0.006 at t = 3000

N, M spectral	$\psi_1\ (r_1, z_1)$	$\psi_2\ (r_2, z_2)$	$\psi_3\ (r_3, z_3)$
64, 96	7.6604×10^{-5}	-7.1496×10^{-3}	1.8562×10^{-5}
	(0.180, 1.96)	(0.760, 0.815)	(0.115, 1.36)
56, 80	7.6589×10^{-5}	-7.1495×10^{-3}	1.8578×10^{-5}
	(0.180, 1.96)	(0.760, 0.815)	(0.115, 1.36)
40, 64	7.6585×10^{-5}	-7.1497×10^{-3}	1.8581×10^{-5}
	(0.180, 1.96)	(0.760, 0.815)	(0.115, 1.36)
40, 56	7.6592×10^{-5}	-7.1498×10^{-3}	1.8582×10^{-5}
	(0.180, 1.96)	(0.760, 0.815)	(0.115, 1.36)
N, M finite difference	$\psi_1\ (r_1, z_1)$	$\psi_2\ (r_2, z_2)$	$\psi_3\ (r_3, z_3)$
120, 300 Stretched	7.5852×10^{-5}	-7.1360×10^{-3}	1.8145×10^{-5}
	(0.186, 1.96)	(0.764, 0.791)	(0.112, 1.36)
120, 300 Uniform	7.3988×10^{-5}	-7.1075×10^{-3}	1.7648×10^{-5}
	(0.183, 1.95)	(0.758, 0.825)	(0.117, 1.35)
60, 150 Stretched	7.4192×10^{-5}	-7.1002×10^{-3}	1.6948×10^{-5}
	(0.186, 1.95)	(0.753, 0.853)	(0.119, 1.33)
60, 150 Uniform	7.1706×10^{-5}	-7.0783×10^{-3}	1.6588×10^{-5}
	(0.183, 1.95)	(0.767, 0.800)	(0.117, 1.35)

TABLE 3
Local Maxima and Minima of η and Their Locations for Re = 2494, Λ = 2.5, and ε = 0.006 at t = 3000

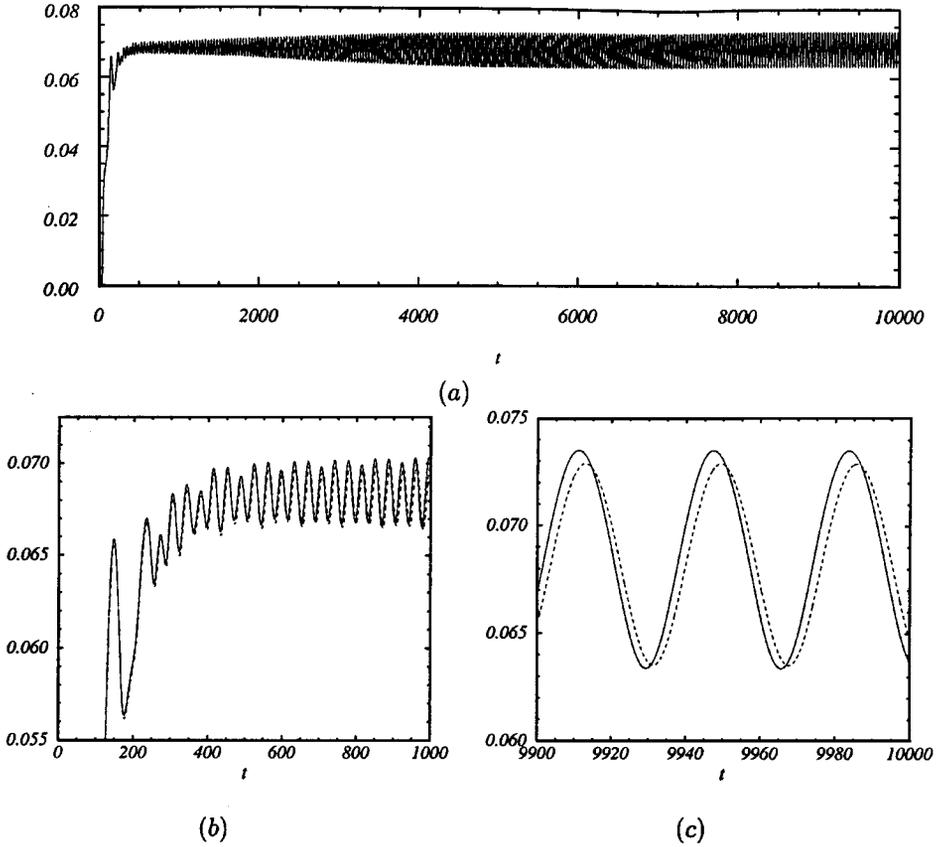| N, M spectral	$\eta_1\ (r_1, z_1)$	$\eta_2\ (r_2, z_2)$	$\eta_3\ (r_3, z_3)$
64, 96	0.54488	-0.52342	-8.9785×10^{-3}
	(0.235, 2.04)	(0.335, 2.28)	(0.0500, 1.91)
56, 80	0.54488	-0.52343	-8.9797×10^{-3}
	(0.235, 2.04)	(0.335, 2.28)	(0.0500, 1.92)
40, 64	0.54494	-0.52341	-8.9683×10^{-3}
	(0.235, 2.04)	(0.335, 2.28)	(0.0500, 1.91)
40, 56	0.54502	-0.52341	-8.8570×10^{-3}
	(0.235, 2.04)	(0.335, 2.28)	(0.0500, 1.92)
N, M finite difference	$\eta_1\ (r_1, z_1)$	$\eta_2\ (r_2, z_2)$	$\eta_3\ (r_3, z_3)$
120, 300 Stretched	0.54146	-0.52045	-8.4318×10^{-3}
	(0.236, 2.04)	(0.329, 2.28)	(0.0498, 1.92)
120, 300 Uniform	0.53590	-0.51547	-7.7323×10^{-3}
	(0.233, 2.03)	(0.333, 2.28)	(0.0500, 1.91)
60, 150 Stretched	0.53166	-0.51282	-7.2154×10^{-3}
	(0.225, 2.05)	(0.341, 2.28)	(0.0498, 1.90)
60, 150 Uniform	0.52433	-0.50879	-6.5468×10^{-3}
	(0.233, 2.033)	(0.333, 2.28)	(0.0500, 1.90)

FIG. 7.   Time histories of $v(r = 1/2, z = \Lambda/2)$ for Re $= 2765$ from computations with the spectral code using $N = 56$, $M = 80$, and $\delta t = 0.04$ (solid line), and the finite difference code using the stretched grids with $N = 120$, $M = 300$, $\delta t = 0.005$ (broken line), Re $= 2765$. (b) and (c) are details of (a).

using the spectral code with $N = 56$, $M = 80$, $\delta t = 0.04$ and the finite difference code with $N = 120$, $M = 300$, $\delta t = 0.005$. Figure 7 gives the time history of $v(r = 1/2, z = \Lambda/2)$. Overall, the two codes agree to about the same extent as they did for the steady case. In particular, the early transients following the impulsive start from rest match very well, as shown in Fig. 7b. Figure 7c gives details of the oscillatory behavior once the limit cycle solution has been established. There is a slight phase shift between the two solutions, but their periods agree quite well. The nondimensional periods are approximately 36.2, and this value is well within the experimental error bounds measured by [35]. The difference in amplitudes of the limit cycles is also of the same order as the difference between the corresponding steady solutions at lower, Re, as noted above.

Finally, a comparison of efficiency is in order. It can be shown and is confirmed by our computations that for a fixed Re the fully discrete semi-implicit second-order projection scheme is unconditionally stable for δt sufficiently small, while the explicit finite difference scheme is only conditionally stable with a stability condition

$$\delta t \lesssim \min\left(\frac{h_{\min}^2}{\text{Re}}, h_{\min}\right),$$

TABLE 4
CPU Seconds Used for 100 Time Steps

$N, M, \delta t$	Code	CPU seconds for 100 time steps
64, 96, 0.04	Spectral	20.2
56, 80, 0.04	Spectral	13.6
40, 64, 0.04	Spectral	7.1
40, 56, 0.04	Spectral	6.0
60, 150, 0.05	Finite diff.	12.6
120, 300, 0.025	Finite diff.	58.6

where $h_{\min}$ is the minimum distance between two adjacent grid points. For large Reynolds numbers, as are considered here, the allowable time step for the finite difference code scales like $h_{\min}$. Note that the finite difference codes take the same amount of CPU time per time step for the same (N, M), regardless of the amount of coordinate stretching. The restriction on the time step is more stringent, for the same (N, M), as the coordinate stretching is increased. The time steps used in the computations are all close to the critical time steps.

For a fixed mesh size (N, M), at each time step, the spectral-projection scheme requires the solution of four elliptic equations, whereas the finite difference code only requires two elliptic equations to be solved. We list in Table 4 the CPU seconds used, on one processor of an SGI Power-Challenge R8000, in computing 100 time steps of the two codes at different resolutions. We observe that the CPU time for the spectral-projection code with 57×81 modes is less than one quarter of that used by the finite difference code with 121×301 grid points, while the allowable time step is eight times larger. Thus, for this specific problem, the spectral-projection scheme with 57×81 modes produces a more accurate result at about 3% of the cost of the (stretched) finite difference scheme with 121×301 grid points.

5. CONCLUDING REMARKS

We have presented an efficient, accurate, and stable numerical scheme for the axisymmetric Navier–Stokes equations in primitive variables in a cylinder. The scheme is based on a new spectral-Galerkin approximation [30] for the space variables and a second-order projection scheme for the time variable. In addition to its accuracy and efficiency, the spectral-projection scheme can be readily extended to nonaxisymmetric three-dimensional cases.

We have implemented the scheme to simulate the unsteady incompressible axisymmetric flow driven by a rotating bottom with constant angular speed. We have developed a new procedure which produces mesh independent approximations to the singular boundary condition to within any prescribed accuracy. In problems where physical singularities play an important dynamic role (as a source or sink of vorticity), such as in the present problem and the driven cavity in two-dimensional flows, their treatment is important and the mesh-independent parameter ε may be thought of as a further dynamic parameter describing the flow.

To evaluate the relative merit of the spectral-projection scheme, we have made a sensible comparison with a standard second-order (in time and space) finite difference scheme based on a stream function-vorticity formulation. The two schemes, although totally different in

every aspect, produced very reliable results. Despite the singular boundary condition which is unfavorable to spectral approximations, the spectral-projection scheme is still more accurate (Tables 2 and 3) and more efficient (Table 4) than the finite difference scheme.

APPENDIX A: A STANDARD FINITE DIFFERENCE SCHEME IN STREAM FUNCTION-VORTICITY FORMULATION

The finite difference scheme with which we compare the spectral-projection scheme has been used extensively with success in solving our problem (e.g., [2, 16, 18]) and related problems (e.g., [17, 19]). It solves the governing equations in the ψ, η, Γ formulation, thereby guaranteeing divergence-free flow. The main disadvantage of this formulation is that it does not generalize easily to three dimensions. We now give a brief outline of this scheme.

A Stokes stream function ψ is introduced, along with the angular momentum Γ, so that the velocity and vorticity vectors are now

$$\mathbf{u} = \left(-\frac{1}{r}\psi_z, \frac{1}{r}\Gamma, \frac{1}{r}\psi_r \right)$$

and

$$\boldsymbol{\omega} = \left(-\frac{1}{r}\Gamma_z, -\frac{1}{r}\nabla_*^2\psi, \frac{1}{r}\Gamma_r \right),$$

where

$$\nabla_*^2 = \partial_r^2 - \frac{1}{r}\partial_r + \partial_z^2.$$

In terms of ψ, η, and Γ, the axisymmetric Navier–Stokes equations (1.1)–(1.3) become

$$D\Gamma = \frac{1}{\text{Re}}\nabla_*^2\Gamma, \tag{A.1}$$

$$D(\eta/r) = \frac{1}{\text{Re}}\left[\nabla^2(\eta/r) + \frac{2}{r}(\eta/r)_r \right] + (\Gamma^2/r^4)_z, \tag{A.2}$$

$$-\nabla_*^2\psi = r\eta, \tag{A.3}$$

where

$$D = \partial_t - \frac{1}{r}\psi_z\partial_r + \frac{1}{r}\psi_r\partial_z.$$

The boundary and axis conditions are that $\psi = 0$ on all walls and the axis, and the normal and tangential derivatives of ψ on all walls are zero; $\Gamma = 0$ on all stationary walls and the axis, $\Gamma = r^2$ on the rotating endwall; and $\eta = 0$ on the axis.

The main difficulty associated with the stream function-vorticity formulation is the lack of the vorticity boundary condition, as opposed to the lack of pressure boundary condition for the primitive variable formulation. However, this difficulty can be overcome by using an explicit time discretization for (A.1)–(A.2) described below.

We first discretize Eqs. (A.1)–(A.3) in space by using second-order centered differences at grid points (r_i, z_j) for $i = 1, \ldots, N - 1$ and $j = 1, \ldots, M - 1$ ($i = 0$ or N or $j = 0$ or M represent the points on the boundary), resulting in a system

$$\partial_t \Gamma_{ij} = G_1(\Gamma_{ij}, \eta_{ij}, \psi_{ij}) \tag{A.4}$$

and

$$\partial_t \eta_{ij} = G_2(\Gamma_{ij}, \eta_{ij}, \psi_{ij}), \tag{A.5}$$

$$-\nabla_*^2 \psi_{ij} = r_i \eta_{ij}, \tag{A.6}$$

where G_1 and G_2 represent the finite difference approximations for all the terms except the one with time derivative in (A.4) and (A.5), respectively.

For the problem we are considering, the dynamics are dominated by the structure of the boundary layers, and an efficient resolution of these using finite differences requires a nonuniform grid stretched near the boundary. In the comparison with the spectral scheme, we consider both uniform and stretched grids, where the radial stretching function is given by

$$r = x - a \sin(2\pi x),$$

and the axial stretching function is given by

$$z = \Lambda(y - b \sin(2\pi y)),$$

where $x, y \in [0, 1]$ and a and b are constants, taken here to be 0.1.

We now use a second-order predictor–corrector scheme to discretize in time so that the boundary condition for ψ on the walls gives that $\eta = (1/r)\psi_{nn}$ on all walls (here the subscript n denotes differentiation normal to the wall). More precisely, the scheme is implemented in the following fashion:

1. Evaluate

$$\Gamma_{ij}^* = \Gamma_{ij}^k + 0.5\delta t \, G_1\left(\Gamma_{ij}^k, \eta_{ij}^k, \psi_{ij}^k\right),$$

and

$$\eta_{ij}^* = \eta_{ij}^k + 0.5\delta t \, G_2\left(\Gamma_{ij}^k, \eta_{ij}^k, \psi_{ij}^k\right),$$

for $i = 1, \ldots, N - 1$ and $j = 1, \ldots, M - 1$.
2. Solve $\nabla_*^2 \psi_{ij}^* = -r \eta_{ij}^*$.
3. Implement boundary conditions on Γ^* and η^*.
4. Evaluate

$$\Gamma_{ij}^{k+1} = \Gamma_{ij}^k + \delta t \, G_1\left(\Gamma_{ij}^*, \eta_{ij}^*, \psi_{ij}^*\right),$$

and

$$\eta_{ij}^{k+1} = \eta_{ij}^k + \delta t \, G_2\left(\Gamma_{ij}^*, \eta_{ij}^*, \psi_{ij}^*\right),$$

for $i = 1, \ldots, N - 1$ and $j = 1, \ldots, M - 1$.

5. Solve $\nabla_*^2 \psi_{ij}^{k+1} = -r\eta_{ij}^{k+1}$.
6. Implement boundary conditions on Γ^{k+1} and η^{k+1}.
7. Goto the next time step.

To solve the Poisson equations in steps (2) and (5) we only require knowledge of η on the interior grid points, i.e. $i = 1, \ldots, N-1$ and $j = 1, \ldots, M-1$. The Poisson equations can be efficiently solved by the generalized cyclic reduction routine BLKTRI from the FISHPACK package [36], whose computational complexity is of order $NM \log_2 N$ or by using the matrix diagonalization method [22] whose computational complexity is of order $NM \min(N, M)$. However, the relative performance of the two approaches will depend on the grid size, the machine architecture, and the availability of machine coded BLAS (basic linear algebra subroutines).

ACKNOWLEDGMENTS

REFERENCES

1. J. Bell, P. Colella, and H. Glaz, A second-order projection method for the incompressible Navier–Stokes equations, *J. Comput. Phys.* **85**, 257 (1989).

2. G. L. Brown and J. M. Lopez, Axisymmetric vortex breakdown, Part 2. Physical mechanisms, *J. Fluid Mech.* **221**, 553 (1990).

3. C. Canuto, M. Y. Hussaini, A. Quarteroni, and T. A. Zang, *Spectral Methods in Fluid Dynamics* (Springer-Verlag, New York/Berlin, 1987).

4. A. J. Chorin, Numerical solution of the Navier–Stokes equations, *Math. Comput.* **22**, 745 (1968).

5. O. Daube and J. N. Sørensen, Simulation numérique de l'écoulement périodique axisymétrique dans une cavité cylindrique, *C.R. Acad. Sci. Paris* **308**, 463 (1989).

6. P. Demaret and M. O. Deville, Chebyshev collocation solution of the Navier–Stokes equations using multi-domain decomposition and finite element preconditioning, *J. Comput. Phys.* **95**, 359 (1991).

7. H. Eisen, W. Heinrichs, and K. Witsch, Spectral collocation methods and polar coordinate singularities, *J. Comput. Phys.* **96**, 241 (1991).

8. M. P. Escudier, Observations of the flow produced in a cylindrical container by a rotating endwall, *Expts. Fluids* **2**, 189 (1984).

9. G. Georgiou, L. G. Olson, W. W. Schultz, and S. Sagan, A singular finite element for Stokes flow: The stick-slip problem, *Int. J. Numer. Methods Fluids* **9**, 1353 (1989).

10. D. Gottlieb and S. A. Orszag, *Numerical Analysis of Spectral Methods: Theory and Applications* (SIAM-CBMS, Philadelphia, 1977).

11. J. E. Hart and S. Kittelman, Instabilities of the sidewall boundary layer in a differentially driven rotating cylinder, *Phys. Fluids* **8**, 692 (1996).

12. J. E. Hart and M. D. Mundt, Instability of oscillatory Stokes-Stewartson layers in a rotating fluid, *J. Fluid Mech.* **311**, 119 (1996).

13. J. G. Heywood and R. Rannacher, Finite element approximation of the nonstationary Navier–Stokes problem, III. Smoothing property and higher order estimates for spatial discretization, *SIAM J. Numer. Anal.* **25**, 489 (1988).

14. C. C. Jahnke and D. T. Valentine, Boundary layer separation in a rotating container, *Phys. Fluids* **8**, 1408 (1996).

15. H. C. Ku, R. S. Hirsh, and T. D. Taylor, A pseudospectral method for solution of the three-dimensional incompressible Navier–Stokes equations, *J. Comput. Phys.* **70**, 439 (1987).

16. J. M. Lopez, Axisymmetric vortex breakdown, Part 1. Confined swirling flow, *J. Fluid Mech.* **221**, 533 (1990).

17. J. M. Lopez, Flow between a stationary and a rotating disk shrouded by a co-rotating cylinder, *Phys. Fluids* **8**, 2605 (1996).

18. J. M. Lopez and A. D. Perry, Axisymmetric vortex breakdown, Part 3. Onset of periodic flow and chaotic advection, *J. Fluid Mech.* **234**, 449 (1992).

19. J. M. Lopez and P. D. Weidman, Stability of stationary endwall boundary layers during spin-down, *J. Fluid Mech.* **326**, 373 (1996).

20. H. J. Lugt and M. Abboud, Axisymmetric vortex breakdown with and without temperature effects in a container with a rotating lid, *J. Fluid Mech.* **179**, 179 (1987).

21. H. J. Lugt and H. J. Haussling, Development of flow circulation in a rotating tank, *Acta Mech.* **18**, 255 (1973).

22. R. E. Lynch, J. R. Rice, and D. H. Thomas, Direct solution of partial differential equations by tensor product methods, *Numer. Math.* **6**, 185 (1964).

23. T. Matsushima and P. S. Marcus, A spectral method for polar coordinates, *J. Comput. Phys.* **120**, 365 (1995).

24. G. P. Neitzel, Streak-line motion during steady and unsteady axisymmetric vortex breakdown, *Phys. Fluids* **31**, 958 (1988).

25. S. A. Orszag, Fourier series on spheres, *Monthly Weather Rev.* **102**, 56 (1974).

26. H. P. Pao, Numerical solution of the Navier–Stokes equations for flows in the disk-cylinder system, *Phys. Fluids* **15**, 4 (1972).

27. B. Ronnenberg, *Ein selbstjustierendes 3-komponenten-LDA nach dem vergleichsstrahlverfahren, angewendt für untersuchungen in einer stationaren zylindersymmetrischen drehströhmung mit einen rückströmgebiet*, Technical Report Bericht 20, Max-Planck-Institut für Strómungsforschung, Gottingen, 1977.

28. W. W. Schultz and C. Gervasio, A study of the singularity in the die swell problem, *Q.J. Mech. Appl. Math.* **43**, 407 (1990).

29. W. W. Schultz, Lee, and J. P. Boyd, Chebyshev pseudospectral method of viscous flows with corner singularities, *J. Sci. Comput.* **4**, 1 (1989).

30. J. Shen, Efficient spectral-Galerkin methods III, Polar and cylindrical geometries, *SIAM J. Sci. Comput.* **18**, 1583 (1997).

31. J. Shen, Hopf bifurcation of the unsteady regularized-driven cavity flows, *J. Comput. Phys.* **95**, 228 (1991).

32. J. Shen, Efficient Chebyshev-Legendre Galerkin methods for elliptic problems, in *Proceedings of ICOSA-HOM'95*, edited by A. V. Ilin and R. Scott, pp. 233–240. [*Houston J. Math.* (1996)]

33. J. Shen, On error estimates of projection methods for the Navier–Stokes equations: Second-order schemes, *Math. Comput.* **65**, 1039 (1996).

34. J. N. Sørensen and E. A. Christensen, Direct numerical simulation of rotating fluid flow in a closed cylinder, *Phys. Fluids* **7**, 764 (1995).

35. J. L. Stevens, J. M. Lopez, and B. J. Cantwell, Oscillatory flow states in an enclosed cylinder with a rotating endwall, *J. Fluid Mech.* (1997), submitted.

36. P. N. Swarztrauber and R. A. Sweet, Efficient FORTRAN subprograms for the solution of elliptic partial differential equations, *ACM Trans. Math. Soft.* **5**, 352 (1979).

37. R. Temam, Sur l'approximation de la solution des équations de Navier–Stokes par la méthode des pas fractionnaires ii, *Arch. Rat. Mech. Anal.* **33**, 377 (1969).

38. N. Tsitverblit, Vortex breakdown in a cylindrical container in the light of continuation of a steady solution, *Fluid Dyn. Res.* **11**, 19 (1993).

39. L. S. Tuckerman, Divergence-free velocity fields in nonperiodic geometries, *J. Comput. Phys.* **80**, 403 (1989).

40. J. van Kan, A second-order accurate pressure-correction scheme for viscous incompressible flow, *SIAM J. Sci. Stat. Comput.* **7**, 870 (1986).

41. H. U. Vogel, *Experimentelle ergebnisse úber die laminare strömung in einem zylindrischen gehaüse mit darin rotierender scheibe*, Technical Report Bericht 6, Max-Planck-Institut für Strómungsforschung, Gottingen, 1968.